Applied Materials Today 40 (2024) 102365

Contents lists available at ScienceDirect

Applied Materials Today

journal homepage: www.elsevier.com/locate/apmt

Inkjet assisted electroforming and collective actuation of disk-shaped magnetic micromotors

Roberto Bernasconi [a,*], Anna Nova [a], Buse Aktas [b], Salvador Pané [b], Luca Magagnin [a]

[a] Dipartimento di Chimica, materiali e Ingegneria Chimica "Giulio Natta", Politecnico di Milano, Via Mancinelli 7, 20131, Milano, Italy
[b] Multi-Scale Robotics Lab, Institute of Robotics and Intelligent Systems, ETH Zurich, Tannenstrasse 3, CH-8092, Zürich, Switzerland

ARTICLE INFO

Keywords:
Inkjet
Lithography
Ferromagnetic
Micromotors
Swarm

ABSTRACT

Microrobotic swarms, with their intrinsic ability to multiply the properties of a single device by hundreds or thousands of times, demonstrate great potential for advanced microsurgery, targeted drug delivery or manipulation at the microscale. This is especially true in the case of magnetically actuated swarms, which can be remotely manipulated with high precision also in-vivo. The manufacturing and the collective actuation of a large number of devices, however, is a challenging task and it requires the development of highly tailored, adaptable and low cost strategies. In the present work, we demonstrate that a combination of inkjet assisted lithography (IAL) and electroforming can be a high-throughput, scalable and low-cost fabrication method for the production of disk-shaped ferromagnetic micromotors. Thanks to the versatility of the hybrid manufacturing technique developed, the diameter and the thickness of the devices can be easily controlled and tailored according to the target application. In addition, the use of electroforming makes possible the manufacturing of soft or hard magnetic devices, whose magnetization direction can be programmed. In the specific case, Ni and CoNiP devices were produced, characterized and actuated in swarms composed of hundreds of individuals. According to their magnetic properties, the devices exhibited highly controllable actuation patterns with multiple degrees of freedom. In order to provide an applicative perspective, the ferromagnetic micromotors were coated with polypyrrole and employed for drug delivery, evidencing thus their capability to load and release the model molecule Rhodamine B.

1. Introduction

Mobile microrobots are untethered devices with micrometric dimensions, characterized by self-contained capabilities for locomotion, sensing, and functional operations [1]. They find application in a variety of fields, ranging from biomedical engineering to environmental remediation, micro-manipulation or even targeted drug delivery [2]. Their size range includes the average dimensions of a mammalian cell, allowing direct access to delicate body sites and minimal tissue damage during medical interventions [3,4]. Magnetic actuation is a widespread method to control microrobots in such environments since magnetic fields can penetrate tissues without adverse reactions. In addition, different magnetic actuation techniques have been developed, based on three driving principles: the magnetic field gradient, the rotating magnetic field, and the oscillating magnetic field [5]. These can be easily applied using arrays of electromagnetic coils like the OctoMag, which is composed of eight stationary electromagnets and allows a five degrees of freedom (5-DOF) wireless magnetic control of fully untethered microrobots [6].

Among all possible fields of application, bioengineering and, in particular, drug delivery, are the sectors on which the impact of microrobots could be the highest [7]. Targeted release seems a promising technique to overcome the limitations of conventional drug delivery methods. It consists in conveying the medication selectively to the site where it is meant to act, in order to localize its interaction with the diseased cells and to avoid any possible harmful effect to healthy tissue. By avoiding the dispersion of the drug in the body it is possible to decrease the intake frequency; furthermore, since active principles are often unstable, reducing the time required to reach the site of interest increases the effectiveness of the treatment [8]. Polypyrrole (PPy) is one of the mostly employed materials to provide the microrobots with the drug delivery function. Using this polymer, Sivaraman et al. [9] realized wirelessly controlled magnetic microrobots designed to treat pathologies in the posterior part of the human eye. By applying alternating

* Corresponding author.
E-mail address: roberto.bernasconi@polimi.it (R. Bernasconi).

https://doi.org/10.1016/j.apmt.2024.102365
Received 2 March 2024; Received in revised form 25 June 2024; Accepted 27 July 2024
Available online 13 August 2024

magnetic fields, eddy currents were generated on the surfaces of these devices. This increased the surface temperature and acted as a remote trigger for the release of the drug. Bernasconi et al. [10] fabricated 3D printed and PPy coated microdevices aimed at providing localized drug administration for the therapy of many diseases typical of the gastrointestinal tract.

Considering the size difference among microrobots and their targets, such as tissues and organs, the capacity of an individual microrobot would be insufficient for achieving desired effects at the macroscale (≈ 1 cm). In particular, considering drug delivery applications, the loading capability for drugs of a single microrobot may meet a critical limitation, due to the small size and volume of the device itself. At the same time, the real time in vivo imaging of a single microrobotic agent could also result very challenging. To tackle these problems, swarm actuation and control strategies of groups of devices have started to be investigated [11–13]. Also, microrobotic swarms can maintain a precise pattern during locomotion and perform pattern reconfigurations, which allows them to fit inside complex environments to reach the target [14]. Obviously, the controlled actuation of a swarm is not trivial and many different approaches have been proposed to pattern and synchronize the movement of hundreds or thousands of mutually interacting devices. These include the use of light [15–20], ultrasounds [21,22], chemical reactions [23,24] or magnetic fields [25–28]. For what concerns magnetically actuated systems, Yu et al. [29] realized swarms from paramagnetic magnetite nanoparticles with a diameter of 100 nm. To disassemble the particle clusters, they applied a dynamic oscillating field characterized by a complex rotatory movement. Subsequently, they realized a vortex-like swarm by applying a rotating magnetic field [30]. Ribbon-like swarms were also obtained by applying a magnetic field oscillating on a single plane and with a defined angle [31]. Both swarms can perform navigated locomotion by applying magnetic fields with pitch angles. Interesting results were also obtained by Sing et al. [32], who realized self-organized and reconfigurable microrobotic swarms with programmable collective order, by Xie et al. [33], who employed alternating magnetic fields to program colloidal particles into liquid, chain, vortex and ribbon-like microrobotic swarms and by Xu et al., who studied the simultaneous actuation of multiple flexible devices [34].

From the manufacturing point of view, microrobots generally requires complex and expensive technologies, such as two-photon stereolithography [35], physical evaporation [24] or techniques originally borrowed from the integrated circuit industry [36]. The present research proposes a new flexible and cost-effective fabrication process for microrobotic swarms, achieved through a novel combination of electroplating and inkjet printing. Inkjet printing allows the printing of micrometric features with high resolution in a simple and cost-effective way, making the technology appealing to microrobotics [37]. For micron sized features, this translates into the possibility of lithography-free patterning. In addition, inkjet printing allows to perform inverse patterning, an interesting principle investigated in many studies. For example, Bao et al. [38] developed a method to inkjet print concave microstructures with high resolution, while Sele et al. [39] presented a self-aligning technique that is capable of defining sub-100 nm features, with two simple additive printing steps. Despite these promising researches, inkjet printing has not yet been investigated for the fabrication of microrobots. In this work, a first possible application of this technology in the manufacturing of microdevices is proposed. The process proposed is inspired by inverse patterning but exploits a UV-curable photoresist.

The hybrid methodology here developed could be referred to as Inkjet Assisted Lithography (IAL) and consists in the realisation, through inkjet printing, of a polymeric mask meant to act as a template for metal electrodeposition. In this way, the fabrication steps and the equipment connected to lithography (mask makers, mask aligners …) are not required anymore, with relevant advantages in terms of cost and ease of production. The polymeric mask is made of SU-8, an epoxy-based photoresist, originally developed for microelectronics applications, characterized by good mechanical and chemical resistance and by optimal biocompatibility [40]. The inkjet printing of this material has been widely studied, and applied to the realization of electronic devices, MEMS and, in general, micrometric features [41–43]. The IAL methodology described in the present work is characterized by a high versatility for what concerns patterning. Indeed, the manuscript describes the IAL of circular shapes, but also complex patterns and geometries can also be transferred, going beyond a single droplet. In addition, the manufacturing procedure proposed allows the production of the devices using different metallic materials. Two model materials, characterized by different magnetic behaviours, were selected: nickel, which is soft ferromagnetic, and CoNiP, which is semi-hard. However, other soft and hard ferromagnetic materials can be potentially employed, including equiatomic FePt, which would be an interesting choice for biomedical applications thanks to its biocompatibility. This alloy can be easily electrodeposited, even from non-aqueous electroplating baths [44].

As a second main aim of the work, microrobots behavior during magnetic actuation was studied, considering the collective locomotion of articulated swarms. The influence of the ferromagnetic properties of the materials on actuation patterns was evaluated and characterized. Finally, in order to demonstrate the applicability of the resulting devices for medical applications, a swarm of them was utilized for controlled drug release. This function was provided by coating the devices with a polypyrrole layer, and the release performances were evaluated by employing Rhodamine B (RhB) as model molecule. Besides drug delivery, disk shaped micromotors obtained via IAL may find potential applicability also for cancer treatment [45,46] and manipulation/stirring at the microscale [47].

2. Materials and methods

2.1. Substrate preparation for microdevices fabrication

The substrates for the production of the devices were made of copper. Rectangular samples with dimensions equal to 1.6 X 4 cm were cut from silicon wafers coated with a thin copper film (100 nm from sputtering) characterized by a mirror finishing. To increase the thickness of the sputtered copper layer, an additional 5 μm thick film of this metal was electrodeposited from a commercial plating solution (Cuproplus by Tecnochimica). The metal was deposited for a total time of 22 min 30 s at room temperature, at 10 mA cm^{-2} and under mild stirring.

2.2. Inkjet assisted electroforming of the SU-8 mask

Following substrate preparation, the first step of the devices manufacturing process was the realisation of a polymer mask. The photoresist employed was SU-8 2005 (Kayaku Advanced Materials, Inc.). It was distributed on the substrate through spin coating, forming a layer of constant thickness. Following the instructions provided by the producer, the spin coating parameters required to get the desired thickness of 7 μm were the following: initial ramp to 500 rpm with a 100 rpm s^{-1} acceleration and hold for a total of 5 s, then ramp to 1000 rpm with an acceleration of 300 rpm s^{-1} and hold for a total of 30 s. The silver ink droplets were printed on the surface of the SU-8 layer using a Dimatix Materials Printer (DMP) by Fujifilm. The ink was a dispersion of Ag nanoparticles (40% wt., from Sigma Aldrich). The Ag droplets were printed on an area of 10 X 10 mm and with a drop spacing of 200 μm. This lead to a total number of droplets per sample equal to 2500. The printing parameters are summarized in Table 2. The temperature of the DMP plate was kept at 60 °C and the jetting frequency was fixed at 1 Hz. At the end of the printing step, the samples underwent a curing procedure. For the initial soft bake, the temperature was ramped to 65 °C, then kept constant for 1 min, subsequently ramped to 95 °C and kept constant for 2 min. The temperature was gradually decreased to the room value. Following the initial soft bake, the sample was exposed for 2

min to a 9 W UVA light at a distance of 2 cm. Finally, the sample underwent a post-exposure bake, which followed a procedure similar to the soft bake step, (the only difference was the permanence at 95 °C, which was limited to 1 min). The three steps were performed in the dark to avoid uncontrolled SU-8 reticulation. At the end of the reticulation procedure, the uncured polymer was removed by immersing the sample in stirred diethylene glycol methyl ether for 2 min and then rinsed under a vigorous flow of acetone. This development procedure was repeated three times and, at the end, the samples were rinsed with water and dried with nitrogen.

2.3. Metals electrodeposition

The two materials, Ni and CoNiP, for the devices fabrication were grown via electrodeposition inside the holes characterizing the patterned SU-8. Nickel was deposited from Astronickel, a commercial aqueous Watts bath provided by Tecnochimica. The metal was deposited at 20 mA cm^{-2}, 50 °C and with mild stirring. Under these conditions the growth rate was 0.444 μm min^{-1}. A nickel anode was employed and the pH was set at 4.5. To study the properties of the nickel obtained under these conditions, thin layers of metal were deposited onto silicon wafers covered with a 100 nm thick copper layer (Ni was deposited for 3 min). For the realization of the devices, 13 min and 30 s of deposition were required to achieve a nickel thickness of 6 μm. Since the total surface area of the devices was 0,071 cm^2 (calculated according to Eq. (1) and considering a diameter D for the single device equal to 60 μm), the necessary current was 1.42 mA.

$$A_{total} = A_{single\ device} \cdot 2500 = \pi \frac{D^2}{4} \cdot 2500 \quad (1)$$

In the case of patterns with different diameter of the holes, the current was kept equal to this value, in order to have in all the devices the same quantity of metal regardless of the diameter. As a result, smaller microrobots resulted thicker and larger ones thinner.

CoNiP was deposited, without stirring, from the following bath: 200 mM $NiCl_2 \cdot 6H_2O$, 125 mM $CoCl_2 \cdot 6H_2O$, 146 mM $NaH_2PO_2 \cdot H_2O$, 700 mM NaCl, 400 mM H_3BO_3, 5 mM $C_7H_5NO_3S$. The temperature was set at 25 °C, the current was fixed at 10 mA cm^{-2}. A Ni anode was employed during the deposition. CoNiP was deposited in reverse pulse plating (RPP) mode, exploiting a pulse cycle similar to the one described by Pané et al. [48], constituted by a cathodic pulse at 10 mA cm^{-2} with a pulse duration of 1 ms, followed by an anodic pulse at 5 mA cm^{-2} with a pulse duration of 1 ms. As it was done with nickel, to study the magnetic properties, the CoNiP alloy was deposited on silicon wafers covered with a 100 nm thick copper layer (CoNiP was deposited for 15 min). The deposition of CoNiP in the SU-8 template was performed considering the same area used for Ni. Consequently, the cathodic current for the RPP process was set at 0.71 mA, while the anodic current was set at 0.355 mA. Deposition was carried out for 3600 s. Following metals deposition, the SU-8 mask was removed by immersing the samples in n-methyl-2--pyrrolidone (NMP), at 60 °C and with stirring, until complete detachment of the SU-8 layer.

2.4. Release from the substrate

Ni devices were detached from the substrate by immersing the samples in a commercial solution specifically designed to selectively dissolve copper, Copper Etch 49–1 by Transene Company. Once released, the devices were collected with a NdFeB permanent magnet and washed with demineralized water. For CoNiP devices, an alkaline selective etchant for copper was prepared. 1 ml of hydrogen peroxide was mixed with 5 ml of a 32 wt% ammonia solution and water was added until reaching the volume of 100 ml. Once released, the devices were collected and washed as in the previous case. At the end of the washing steps, all the devices were collected from the beaker using a micropipette and stored under water in vials.

2.5. Surface functionalization with polypyrrole

Some nickel devices were coated with polypirrole (PPy). The synthesis of PPy took place thanks to an in situ oxidative polymerisation reaction, in which APS works as oxidant and citric acid as dopant [49]. Such reaction was carried out at 0–5 °C to properly control the polymerization rate of pyrrole. Ice was employed to cool a bath in which the beaker containing the devices and the coating solution was immersed. The solution was constituted of 200 mM citric acid, 1 mM pyrrole and 1 mM ammonium persulfate (APS), all dissolved in 100 ml demineralized water [50]. The devices were dispersed in the solution when it contained only the citric acid and the pyrrole. They were kept in suspension using an immersion stirrer, equipped with a glass propeller and set at 500 rpm. APS was then added drop by drop. In order for the reaction to fully develop, four hours were needed. At the end of the process, samples were collected with a magnet, washed three times and placed in a vial containing water.

2.6. Magnetic actuation

The magnetic actuation of the devices was performed using the NanoMag. With this instrument, analogous to the OctoMag [6], it is possible to control the application of variable magnetic fields and gradients inside a specific volume located at the centre of the system. In the present case, the actuation was realized through magnetic fields rotating around the three Cartesian axes. The control was exerted by changing the intensity of the applied field, its rotational frequency and the orientation of its axis of rotation. Actuation tests were performed in water, low viscosity silicone oil (5 cSt) or high viscosity silicone oil (100 cSt). To host the devices, a circular arena with a diameter of around 5 mm was realized on a microscope slide. The devices were placed inside the arena together with a few droplets of the medium in which the test was meant to be performed; then the arena was positioned inside the NanoMag.

2.7. Magnetic programming of CoNIP devices

To program the magnetization direction of the CoNiP devices, a swarm was placed in the circular arena used for actuation, which was filled with water. The arena was placed in a refrigerator until the water totally froze. Then, a cylindrical NdFeB permanent magnet (10 cm diameter and 1 cm thickness) was placed in contact with the back of the arena and then removed. The diameter of the magnet (10 cm) was considerably larger than the diameter of the arena containing the devices (5 mm). This aspect guaranteed that the magnetic field was uniform in correspondence of the devices. Finally, ice was melted at room temperature.

2.8. Drug release tests

In order to study the drug release functionality introduced on the PPy coated Ni devices, drug release tests were performed according to a standard procedure. PPy coated Ni devices were placed in a vial containing a 100 mg/l rhodamine B (RhB) solution for 2 days. Then, the devices were removed from the solution using a pipette, transferred in a clean vial, quickly washed with water and transferred in a third vial containing 400 μl of water. In this last container, the release took place for 2 h at room temperature and without light. Periodical withdrawals were carried out at fixed times. During each withdrawal, the devices were kept on the bottom of the vial using a magnet, while 200 μl of fluid were removed. Immediately after the withdrawal, the volume was reintegrated by adding 200 μl of pure water. The removed fluid was placed in a clean vial and stored in a refrigerator. Spectrophotometry was used to measure the amount of RhB present in each withdrawal. An Infinite 200 PRO spectrophotometer (Tecan) was employed to measure the fluorescence of the samples at 540 nm (two 80 μl samples were

obtained from each withdrawal, resulting thus in two measurements). The results obtained were then elaborated to take into account the withdrawn volumes and normalized according to a calibration curve. Such curve was built using a RhB reference solution (1 mg/l) at the same wavelength.

2.9. Characterisation techniques

The X-rays fluorescence (XRF) setup employed was a Fischerscope by Fischer, the atomic force microscope (AFM) was a NT-MDT Solver Pro and the X-rays diffraction (XRD) instrument was a PW 1830 by Philips

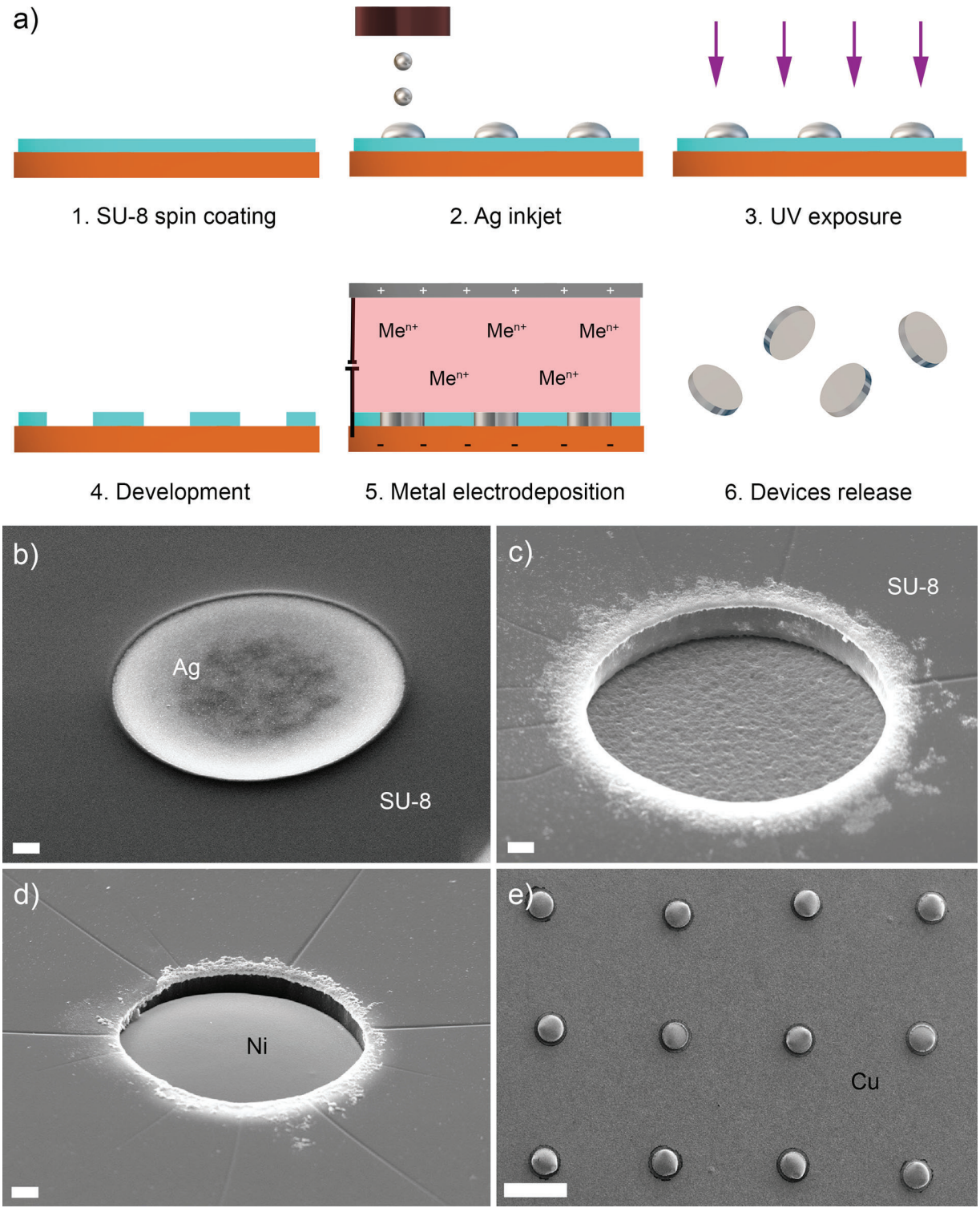

Fig. 1. a) Main steps of the IAL fabrication process on Cu substrate: (1) spin coating of a SU-8 layer on top of the copper sample; (2) inkjet printing of the Ag ink droplets; (3) reticulation of the SU-8 and (4) subsequent removal of the uncured photopolymer laying underneath the droplets; (5) electrodeposition of the selected metal inside the SU-8 pattern; (6) removal of the SU-8 layer and detachment of the devices from the substrate; b) SEM image of the Ag droplets printed on the surface of SU-8 (scale bar = 4 μm); c) SEM image of the cavities left in the polymeric layer after SU-8 developement (scale bar = 4 μm); d) SEM image of one of the cavities constituting the mask with metallic nickel grown inside (scale bar = 4 μm); e) SEM image of nickel devices on Cu substrate, after SU-8 removal (scale bar = 100 μm).

with a PW 3020 goniometer, which employed a Cu-K_α radiation. The scanning electron microscopy (SEM) analysis was carried out using a EVO 50 EP by Zeiss, equipped with an EDS module Model 7060 by Oxford Instruments. The vibrating sample magnetometry (VSM) setup was a MicroMag 3900 by Princeton Measurement Corporation.

3. Results

3.1. Inkjet assisted lithography-based manufacturing process

The main steps of the manufacturing process are summarized through the graphical representation in Fig. 1. After preparing the substrate and spin coating the SU-8 (Fig. 1a, step 1), an array of droplets of Ag ink was printed on the polymeric layer, recreating the shape of the devices. This step, graphically illustrated by the step 2 in Fig. 1a, is documented by the SEM image in Fig. 1b. The employed ink is able to shield the underlying photopolymer from UV light, selectively preventing in this way its reticulation during the following curing step. The printing design is fundamental, because the resulting devices will be cylindrical objects with lateral vertical walls and two planar faces, the shape of which corresponds to that of the Ag droplets printed in this phase. In this work, circular shapes of different diameters were investigated, leading to the realisation of disk-shaped devices. The diameter of the microrobots corresponds to the diameter of the Ag ink droplets. However, it is also possible to pattern and merge ink droplets in order to print more complex shapes. Following the printing step, SU-8 was exposed to UV light (Fig. 1a step 3) and the unreticulated polymer underneath the silver droplets was removed by employing an ultrasonic bath. This step is depicted in the step 4 in Fig. 1a and the result is portrayed in the SEM image of Fig. 1c. The walls of the holes are perfectly vertical, with sharp edges. This means that the UV light was successfully blocked by the Ag droplets and the light source was sufficiently close to the sample to avoid rays hitting the surface at angles different from the normal one. All the incoming UV rays could be therefore considered perpendicular to the plane of the SU-8 layer. It is also possible to detect a thin fissure between the polymeric mould and the Cu substrate. This was probably generated by a non-optimal adhesion between the two layers, which allowed a slight infiltration of acetone during the cleaning step. Subsequently, the desired metal was electrodeposited inside the polymeric pattern (Fig. 1a step 5). The SEM picture in Fig. 1d represents the SU-8 mould filled with electroplated nickel. To obtain CoNiP devices, the same procedure was performed by electroplating CoNiP instead of Ni. The following step consisted in the removal of the SU-8 mask. A SEM image of the devices resulting from this step is presented in Fig. 1e. At the end of the process, the microrobots were detached by employing a selective copper etchant (Fig. 1a step 6). The reason for depositing a 5 μm additional layer of copper on the sputtered copper substrate is connected to this release step of the devices. A thick copper layer, indeed, facilitates its dissolution under the devices, decreasing the time needed for release.

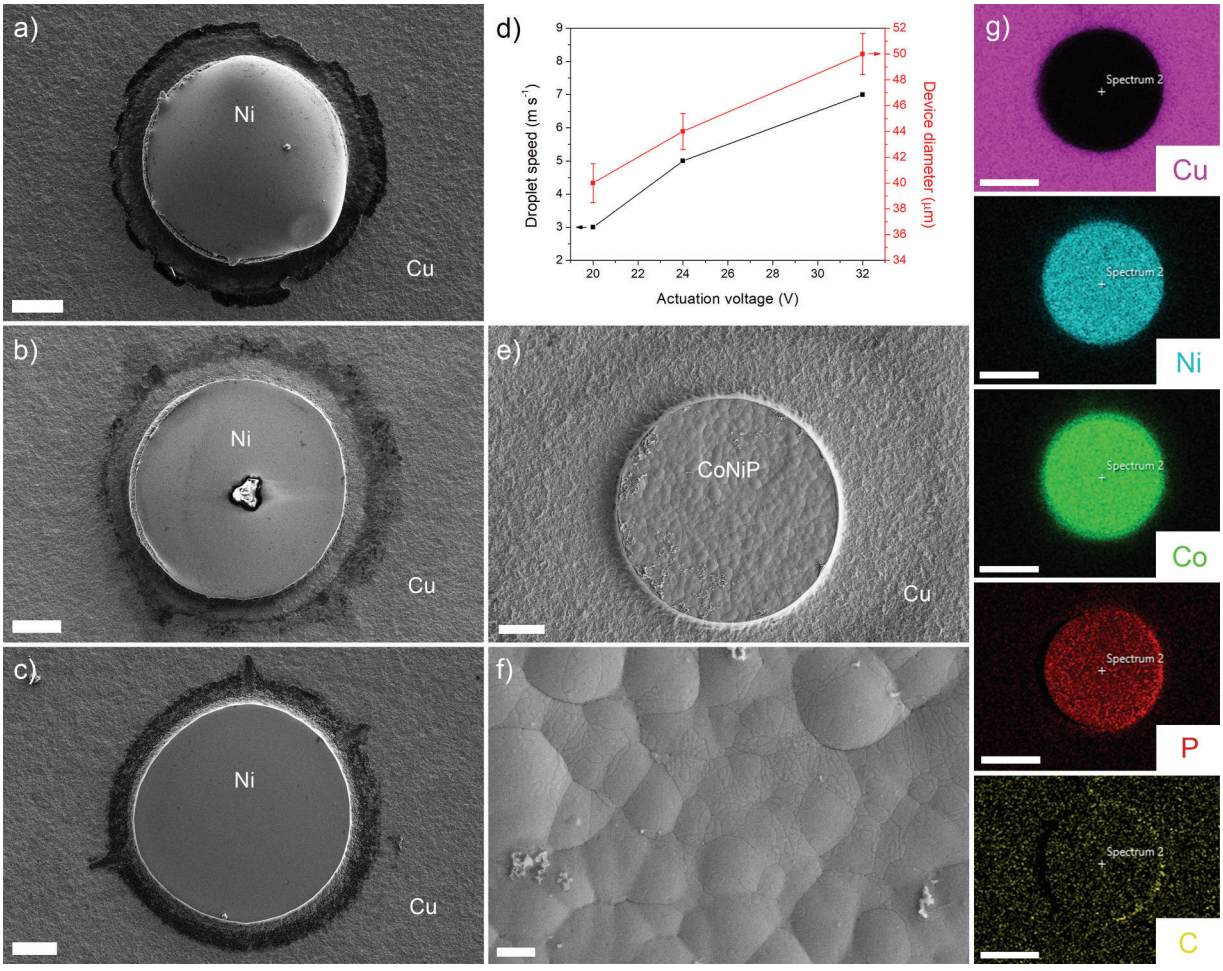

Fig. 2. SEM images of nickel devices on Cu substrate, with diameters of (a) 40 μm (scale bar = 10 μm), (b) 44 μm (scale bar = 10 μm) and (c) 50 μm (scale bar = 10 μm); d) droplet speed and diameter of the final devices as a function of the potential set for the piezoelectric actuator in the inkjet printhead; e) SEM image of a CoNiP device on Cu substrate (scale bar = 10 μm); f) SEM image of the surface of a CoNiP device (scale bar = 1 μm); g) EDS composition maps of a CoNiP device, showing the distribution of Cu, Ni, Co, P and C across the sample (scale bar = 25 μm).

3.2. Dimensions tuning and characterisation of the microdevices

The diameter of the devices can be tuned by changing the speed at which the droplets impact the SU-8 layer (Figs. 2a, 2b and 2c). This speed is dependent on the actuation voltage applied to the piezoelectric element of the printhead (Fig. 2d). Consequently, since the spreading diameter of the Ag ink droplet depends on the speed, also the diameter of the devices is correlated to the jetting voltage applied to the printhead. According to the correspondence reported in Fig. 2d, applied voltages of 20, 24 and 32 V determine droplet speeds of respectively 3, 5 and 7 m s^{-1}, which, in turn, result into diameters of the devices equal to 40 (Fig. 2a), 44 (Fig. 4b) and 50 μm (Fig. 4c). By changing the speed of the droplets, diameters in the 30–60 μm range can be easily obtained (with very low variability for the final diameter of the droplets). However, it is possible to expand the range of printable diameters by using other approaches. For example, alternative printheads can be used. Some models can eject droplets with volumes as high as 400–500 pL, resulting in large diameters, or as low as fractions of pL, resulting in very small diameters. Also the waveform used for the jetting plays a role on the volume of the droplets and, consequently, on the diameter of the printed pattern. Gan et al., for example, tuned the waveform used for jetting a PEDOT solution, obtaining droplet volumes between 70 and 140 pL and final diameters between 60 and 150 μm [51].

The devices fabricated with the procedure described in Section 3.1 have been analysed. Microdevices in nickel were realised in 3 different diameters: 40, 44 and 50 μm. The electroplating current was kept the same in all the cases, equal to 1.42 mA. The volume of magnetic material V, and hence the thickness of the devices at fixed diameter, depends on the total charge used to deposit the metal/alloy according to Faraday's law (Eq. (2)), and consequently on the deposition time.

$$V = \frac{i\,t\,M}{n\,F\,\rho} \tag{2}$$

i is the current employed, t is the deposition time, M is the molar mass of the material deposited, n is its valence, F is the faraday's constant and ρ its density. By keeping constant the deposition time, all the devices were realised with the same quantity of metal, regardless of their diameter. Fig. 2a shows a SEM image of a device with a diameter of 40 μm, Fig. 2b a SEM image of a device with a diameter of 44 μm and Fig. 2c a SEM image of a device with a diameter of 50 μm. The difference in disk thicknesses can be noticed from the comparison between the bulging top surface of the 40 μm-diameter devices and the flat surface of, for example, the 50 μm-diameter ones. Devices with a larger diameter result visibly thinner than the ones with a smaller diameter. The thickness of the disks was calculated by employing Eq. (2) and resulted to be: 8.8 μm for the 40 μm-diameter devices, 7.3 μm for the 44 μm-diameter devices, and 5.7 μm for the 50 μm-diameter devices. The dark ring on the substrate around the devices is probably due to plating solution infiltrations in the fissure highlighted before, between the copper and the SU-8 layer.

Fig. 2e depicts a disk obtained from CoNiP electroplating. For these devices the largest diameter of 50 μm (corresponding to a voltage of 32 V and a droplet speed of 7 m/s) was chosen. For example, the device visible in Fig. 2e has a diameter of 50.10 μm. Considering a 50 μm diameter, the calculated thickness of these devices results to be 5.2 μm. As can be seen from Fig. 2f, the morphology of the surface is compact and uniform, with the characteristic globular structure of electrodeposited CoNiP. Furthermore, no cracks are present on the surface. This is probably a consequence of the reduced dimension of the devices, which cannot accumulate enough internal stresses to develop cracks. The elemental distribution was assessed by means of composition maps. The mapped elements were Cu, Co, Ni, P and C. Thanks to the resulting diagrams, presented in Fig. 2g, it is possible to observe that copper only appears in correspondence of the substrate and that the composition of the CoNiP results uniform across the whole area of the device.

3.3. Materials characterisation

The sample of nickel electrodeposited onto a planar copper substrate was characterized by a mirror-like appearance, thanks to the levelling and brightening agents present in the Ni electroplating bath. The smoothness of the surface was confirmed by SEM (Figure S2) and AFM analysis (Fig. 3a), from which it was possible to calculate a mean roughness (R_a) equal to 1.502 nm. Fig. 3b shows the XRD characterization of the same sample. As visible in Fig. 3b, the phase composition shows a predominance of fcc phase. Its characteristics peaks are clearly visible superimposed to the Cu peaks of the substrate. The magnetic properties of nickel were investigated with the VSM. The resulting analysis is presented in Fig. 3c. The two curves "in plane" and "out of plane" refer to the orientation of the external magnetic field: in the first case parallel and in the second one perpendicular to the surface of the sample. The magnetization was normalized with respect to the volume of the material. From the magnification of the hysteresis loop (Figure S1), it is possible to see that the residual magnetization, even if almost negligible, is however not null. In accordance with the fcc microstructure, Ni exhibits a soft magnetic behaviour. Table 1 reports the magnetic properties of the Ni layer.

The CoNiP alloy was deposited exploiting RPP. The composition of the obtained material, measured via EDS analysis, was the following: 66.28% wt. Co, 28.17% wt. Ni, 5.55% wt. P. The SEM image of the deposit show a homogeneous surface, crossed by a few hairline cracks (figure S3). In general, the structure of the coating is characterized at the nanoscale by a globular morphology. The use of RPP successfully reduces the internal stresses present in the coating, and consequently the density of cracks. Indeed, by using DC, the surface of the alloy resulted to be crossed by a greater number of cracks, that could negatively affect the structural integrity of the layer. RPP is therefore fundamental to produce well-formed microrobots. The AFM analysis shows a uniform layer characterized by a quite low and constant roughness. The R_a is equal to 8.56 nm. In Fig. 3d the AFM three-dimensional image of a 10.5 μm x 10.5 μm area is reported. The XRD characterization is presented in Fig. 3e. Unlike pure Ni, the presence of Co introduces a hcp phase in the CoNiP alloy. Such hcp phase coexists with a fcc phase, whose peaks are evident in the graph. This results are coherent with those reported by Park et al. [52] From the hysteresis loop (Fig. 3f), the information regarding the coercivity and the magnetic remanence of the alloy can be acquired (Table 1). The values of coercivity, in particular, allow to assert the ferromagnetic behaviour of the material. As expectable from the presence of an hcp component in its phase structure, the alloy presents a clear semi-hard magnetic behaviour.

3.4. Interaction between the devices and a static magnetic field

The behaviour of the nickel microrobots in presence of a magnetic field was studied. When the devices are exposed to a static external magnetic field B, they exhibit an expectable behaviour. They tend to self-assembly into long rows composed of a varying number of devices. The reason behind the formation of these rows can be individuated in the behaviour of a disk made of a ferromagnetic material, like nickel, under the influence of an external magnetic field. In general, the external field induces a magnetization M in the material. Due to the strong geometrical anisotropy of the devices, which are characterized by a flat disk shape, the orientation of the induced magnetization vector coincides with the easy axis of a cylinder characterized by a height H much lower that its diameter D. Such easy magnetic axis corresponds, for the symmetry of the cylinder, to any direction perpendicular to the symmetry axis and lying on the mid plane of the cylinder itself (Figure S4). Thanks to the presence of the induced M, the devices behave like small magnets (presenting north and south poles) and stick one after another to form rows of varying length (Fig. 3g). The rows are partially maintained also after removing the external field (Fig. 3h), since the remanence M_r of nickel is not zero (as verified through the VSM

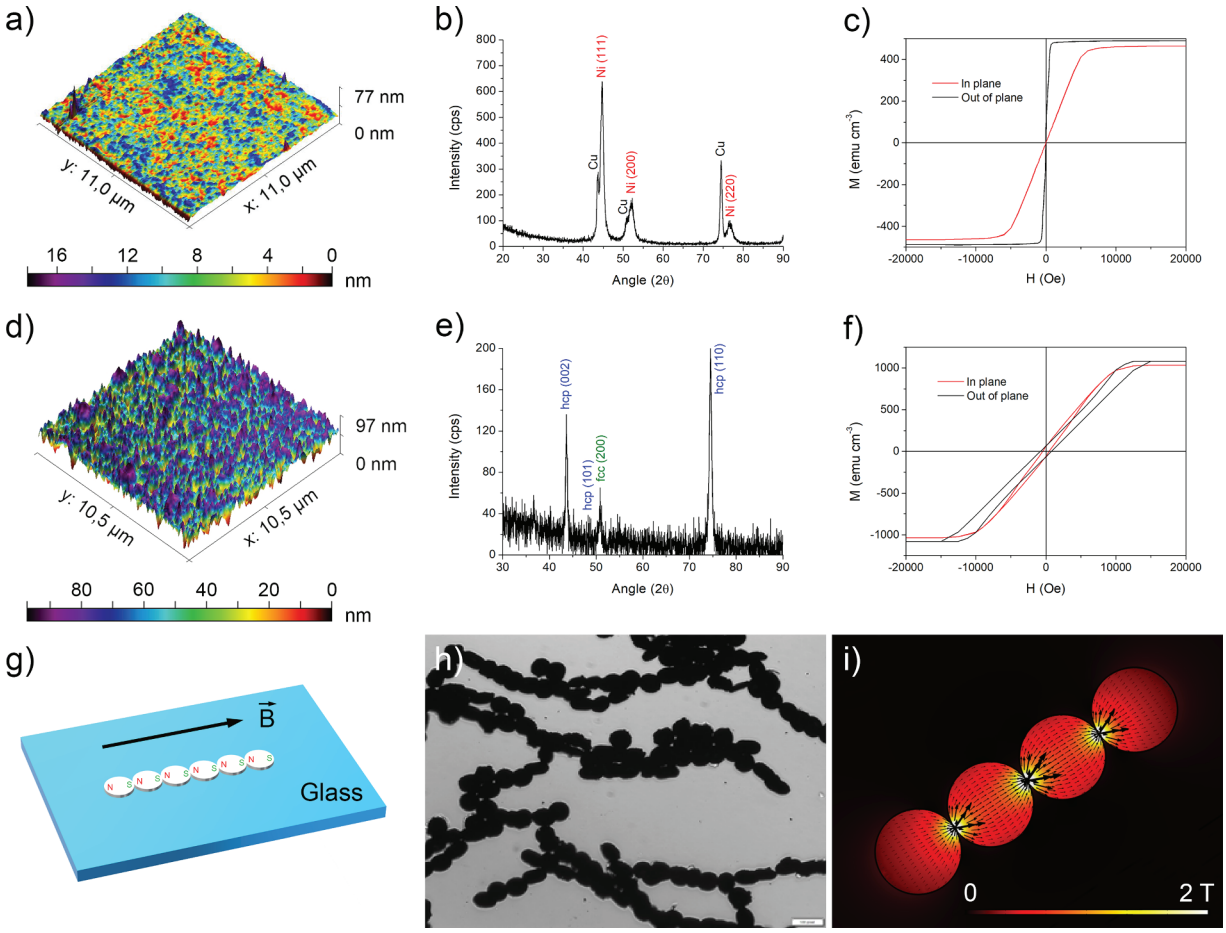

Fig. 3. Characterisation of electrodeposited nickel through AFM (a), XRD (b), VSM (c); characterisation of CoNiP electrodeposited exploiting RPP through AFM (d), XRD (e), VSM (f); g) the chains of devices follow the orientation of the external magnetic field applied; h) self-assembled elongated chains of nickel devices (scale bar = 100 µm); i) FEM simulation of the interaction among 4 devices arranged in a row (applied field = 15 mT).

Table 1
Coercivity H_c, remanence M_r and saturation magnetization M_s of the electrodeposited materials.

	Ni	CoNiP
H_c in plane [Oe]	3	500
H_c out of plane [Oe]	46	833
M_r in plane [emu cm^{-3}]	0.3	54.7
M_r out of plane [emu cm^{-3}]	62.9	64.6
M_s in plane [emu cm^{-3}]	464.2	1032.5
M_s out of plane [emu cm^{-3}]	480.1	1083.3

analysis) and it transforms the devices into weak permanent magnets.

The behavior of the devices can be simulated with a simple FEM model (Fig. 3i). Four Ni devices were placed in a row and subjected to a uniform external magnetic field of 15 mT (a typical value employed for the manipulation of the devices) oriented along the x direction. As visible in Fig. 3i, the magnetization vectors, represented by black arrows, follow the shape of the disks. Indeed, Ni is characterized by a high magnetic permeability, which forces the magnetic field to concentrate in the material and to follow the outer shape of the disks. Consequently, the field also tends to concentrate in the contact points between the devices. In these regions, the magnetization vectors are much stronger than the ones present in the material. The visual representation of the x component of the *B* vector, represented by the colors in Fig. 3i, confirms a significant concentration of magnetic field in correspondence of the point-like zones between a device and the next one. The forces acting on the four disks were evaluated as well and they are reported in Table 2.

Table 2
Evaluation of the forces acting on four devices under a 15 mT magnetic field.

	Force along the x direction (mN)	Force along the y direction (mN)	Force along the z direction (mN)
First device	−0.23349	1.01 E-06	8.63 E-04
Second device	−0.10567	2.09 E-05	1.32 E-04
Third device	0.1073	3.93 E-05	1.28 E-04
Fourth device	0.22958	9.12 E-05	8.72 E-04

As expected, the components of the force along y and z are negligible. Along the x directions, the devices experience negative or positive forces according to their position in the array. This implies that the direction of the forces is a function of the position of the device with respect to the center of gravity of the array. Globally, the resulting force over the array of devices is zero since the magnetic field is uniform. In fact, as evidenced by Eq. (3), only a gradient of magnetic field can induce forces over a magnetic object.

$$\vec{F} = \int_V \left(\vec{M}\cdot\nabla\right)\vec{B}\,dV = V\left(\vec{M}\cdot\nabla\right)\vec{B} \tag{3}$$

Just like a set of macroscopic permanent magnets, the devices exert forces one on the other, whose directions are opposite.

For what concerns the CoNiP devices, under the influence of an

external magnetic field they form chains in a way that is analogous to their Ni counterparts. However, their semi-hard magnetic nature allows them to spontaneously form linear aggregates also in absence of an external field. This effect is due to the presence of a permanent magnetization, imparted during their collection with the NdFeB magnet at the end of the release process. CoNiP is characterized by a significant remanence (Table 1) and the devices can be considered as permanent magnets that autonomously attract and form linear structures.

3.5. Swarm actuation of the Ni devices

As discussed, the disk-shaped devices described in the present work self-organize into rows of variable length. These rows can be moved in a controllable way by applying an oriented or rotating magnetic field. In particular, the key to orient and translate the devices is the application of a torque on the rows. Such torque is a defined by Eq. (4).

$$\vec{T} = \int_V \vec{M} \times \vec{B}\, dV = V\, \vec{M} \times \vec{B} \tag{4}$$

Under the influence of the torque applied, each single row reorients following the direction of the applied field (Fig. 4a). In Fig. 4b, for example, the applied B (having an intensity of 15 mT) was alternatively directed along the three axes. In all the cases, the rows of devices immersed in water followed the direction of the applied field.

Besides controlling the orientation of the rows, the torque can be employed also for their propulsion. By applying a rotating field, a rotating torque can be applied on the devices (Fig. 4c). In this way, the rows are forced to continuously reorient to follow the rotating B, giving rise to a tumbling motion on the surface of the glass substrate [53]. The linear aggregates of disk-shaped devices immersed in water "walk" on the glass substrate (Figure 4d; Supporting Video 1) under the influence of a magnetic field rotating around the x axis, with a speed that is a direct consequence of their length (which is in turn a function of the number of single devices that constitute them). Assuming that the viscous contribution is negligible and that the aggregates are ideally linear, the speed can be expressed by Eq. (5).

$$v = 2DN\varphi \tag{5}$$

v is the linear speed of the aggregate, D is the diameter of a single device, N is the number of devices that constitutes the aggregate and φ is the rotation frequency of the external magnetic field. Obviously, if N increases, also the linear speed of the aggregate increases (Fig. 4e). When the number of devices becomes significant, the aggregates lose their linearity and become more irregular. All maintain an elongated shape, but some present multiple rows of devices joined together. It is also worth pointing out that, since they are constituted by disks that are loosely kept together by magnetic forces, the aggregates continuously reconfigure their shape over time during the actuation. Some of them acquire or loose devices, varying N, and all of them change shape. The aggregates can lose devices due to their excessive length, which can introduce an excessive angular momentum. The rotation can therefore break the aggregate. Finally, the aggregates can impact and merge, since smaller aggregates are slower than larger ones (Figure S5; Supporting Video 2).

Fig. 4f and g report the linear speed of some aggregates as a function of the number of devices they contain and of the magnetic field used for their actuation (Figures S6 and S7 report a magnification of the behavior observed under a 3 mT magnetic field). In all the cases, the speed of the devices increased when N increased. However, it can be noticed that the speed of the aggregates also changed by varying the intensity of the magnetic field used for their actuation. Indeed, the rows actuated at 15 mT travelled at considerable speeds, while the devices actuated at 3 mT were characterized by lower speeds. This is a consequence of the torque applied on the devices (Eq. (4)). If B is not strong enough, the entity of the torque generated is not sufficient to efficiently overcome the viscous drag exerted by water on the aggregates. Consequently, the first assumption for the validity of Eq. (5) (viscous contribution is negligible) is not respected and the devices deviates from the theoretical behavior. The drag force F_d that the aggregate experiences is expressed by Eq. (6).

$$F_d = \frac{1}{2}\, \rho\, v^2\, A\, C_d \tag{6}$$

ρ represents the density of the fluid, v is the speed of the aggregate, A is the active area of the aggregate and C_d is the drag coefficient. When B increases, also T increases and the aggregates can overcome more easily viscous drag. Virtually all the aggregates until N equal to 4 are fully linear and characterized by a small active area A. Therefore, they follow the trend expected (visualized in Fig. 4f and 4g as a green dashed line that represents Eq. (5)) at 15 mT. When N becomes large, the active area A of the devices and their speed v, however, increase and the drag force increases as well. Consequently, they again deviate from the expected behavior. Moreover, when N is high, the aggregates are not fully linear. This is another possible contribution to the deviation from the expected behavior.

The speed of the aggregates changes also when D changes (Eq. (4)). The devices were manufactured in three different dimensions (40, 44 and 50 μm). These three sizes were all actuated in water, yielding the results visible in Fig. 4h. The graph reports the speed of aggregates constituted by a fixed number N of three devices and characterized by a varying D for the disks. In general, the speed increases as D increases, with an acceptable correspondence with the theoretical values identified via Eq. (5).

By considering the results discussed so far, it is evident that the actuation of swarms of disk-shaped ferromagnetic devices is characterized by an important aspect: the differential movement of the chains of disks in terms of speed. Indeed, the swarm of devices contains chains of many different lengths. A typical distribution of these lengths has been calculated in the case of a group of Ni devices actuated at 15 mT / 1 Hz and the result is reported in Fig. 4i. The data demonstrate that the swarm is not constituted by aggregates uniformly having the same length. In turn, it is constituted of single devices, chains with $2 < N < 19$ and very large aggregates with $N \geq 20$. As a consequence, the swarm moves in a differential way, since small aggregates travel at lower speeds than the larger ones. The existence of a range of velocities instead of a single velocity was highlighted also by Yigit et al. [54] in their work, they actuated self-assembled superparamagnetic microparticles into linear chains and they observed that the speed of these chains was a function of the number of beads forming the chain itself.

Another interesting aspect of the actuation of a large number of aggregates, is represented by the inter-aggregate forces. Indeed, the aggregates can be considered as magnets and they can exert a magnetic force on nearby aggregates. The inter-aggregates forces are relevant only at short range. If the aggregates are far apart, their inertia is largely predominant and they are not significantly influenced. However, in a small number of situations, this behavior can be observed (Figure S8).

Further considerations can be done considering the environment where the devices move. By looking at the drag equation (Eq. (6)), it is legitimate to expect also an influence of the viscosity of the fluid on the speed of the devices. The drag coefficient C_d, in fact, is proportional to the Reynolds number Re (Eq. (7)).

$$Re = \frac{\rho v L}{\mu} \tag{7}$$

L is the characteristic length and μ is the dynamic viscosity of the fluid. When the latter increases, Re decreases and the entity of the viscous drag increases. To highlight this effect, a swarm of devices was actuated at 1 Hz in three different fluids: water (whose kinematic viscosity is 1 cSt at 20 °C), low viscosity silicone oil (whose kinematic viscosity is 5 cSt at 20 °C) and high viscosity silicone oil (whose kinematic viscosity is 100 cSt at 20 °C). The results obtained in terms of

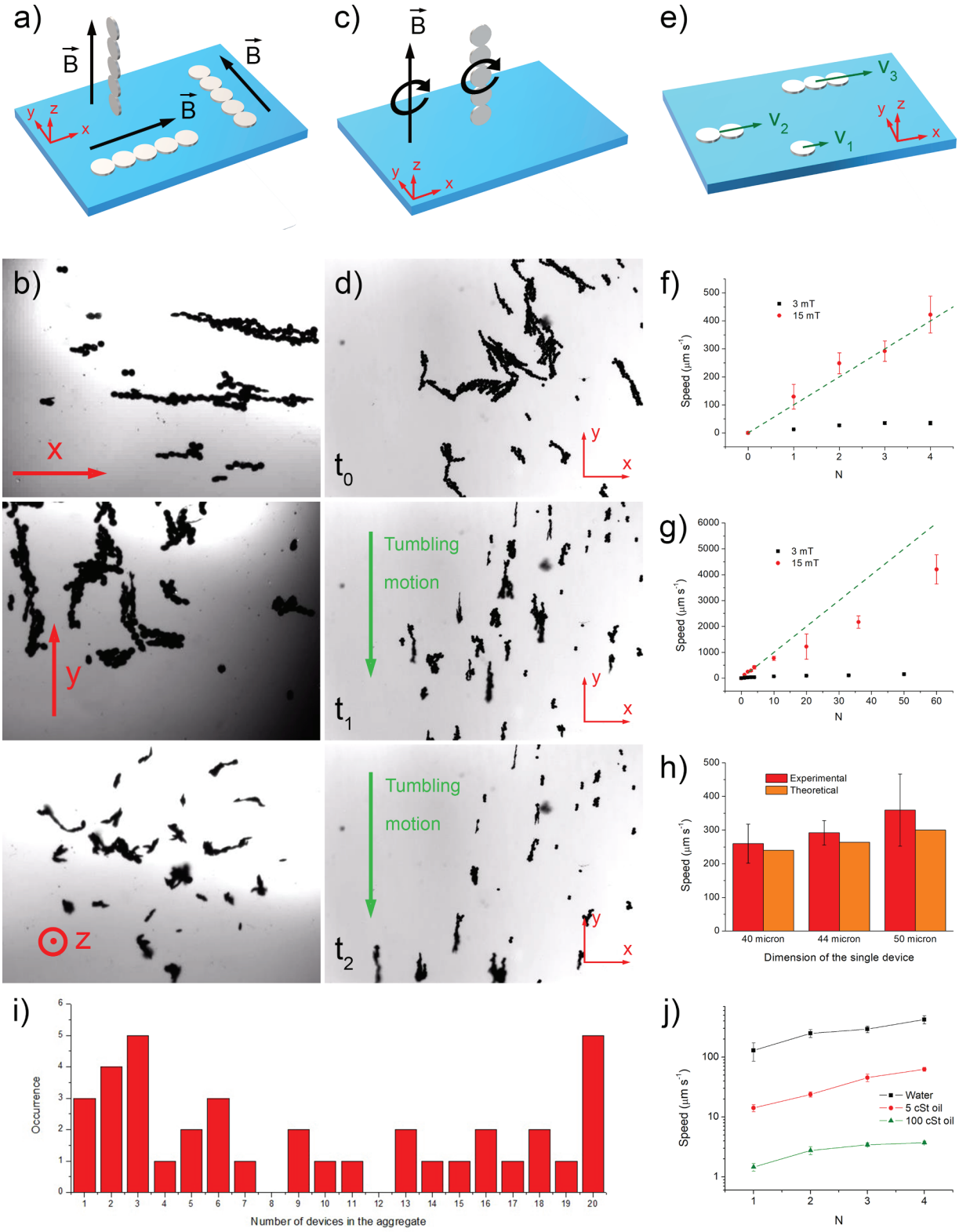

Fig. 4. Scheme (a) and experimental verification (b) of the magnetic alignment of the chains of soft magnetic devices; scheme (c) and experimental verification (d) of the tumbling motion obtained through the application of a rotating magnetic field; scheme for the dependence of linear speed on the number of devices N constituting the aggregates (e); experimental evaluation of the relationship between the linear speed and the number of devices N constituting the aggregates for small (f) and large (g) values of N; relationship between linear speed and diameter of the single device D (h); size distribution of the aggregates observed during a typical actuation test (i); relationship between linear speed and viscosity of the actuation environment (j).

linear speed vs. dimension of the aggregates actuated are reported in Fig. 4j. The effect of viscosity is evident, with a variation in the final speed of roughly one order of magnitude moving from one fluid to the other. The effect of viscosity can be visually appreciated also by watching Supporting Video 2.

3.6. Swarm actuation of the CoNiP devices

The second class of devices described in the present work comprises disks made of CoNiP. This alloy, as evidenced by the VSM analysis carried out (Fig. 3f), is characterized by semi-hard magnetic properties, which include the possibility to obtain a stable high magnetization. The latter, thanks to the good remanence of the material, also allows the creation of relatively strong permanent magnets.

The CoNiP devices can be actuated exactly in the same way as their Ni counterparts. Considering the number of devices constituting aggregates N, its effect on final speed is analogous to the Ni devices (figures S9 and 5a; Supporting Video 3). However, due to their higher magnetization M, higher values of torque can be efficiently applied during their actuation (Eq. (4)). This effect can be observed at high actuation speed (and consequently rotation frequency ν). The effect of a higher M is visible in Fig. 5b, which reports the speed of a single device, alternatively made of Ni or CoNiP, under the effect of a 15 mT magnetic field rotating at different frequencies. It can be observed that the Ni device reached a maximum in its speed when the frequency was around 5 Hz. Then, at higher frequencies, its velocity dropped and stabilized on a 100 μm s^{-1} plateau. This behavior presents strong analogies with the step-out phenomenon experienced by artificial bacterial flagella (ABFs) [55,56]. These helical structures are propelled by rotating magnetic fields and, at low rotation frequencies, their motion properly follows the external field. In general, their linear speed presents a maximum value, above which it reduces with increasing field frequency. The explanation for this phenomenon is that the available magnetic torque (Eq. (4)) is no longer enough to totally overcome the viscous forces acting on the

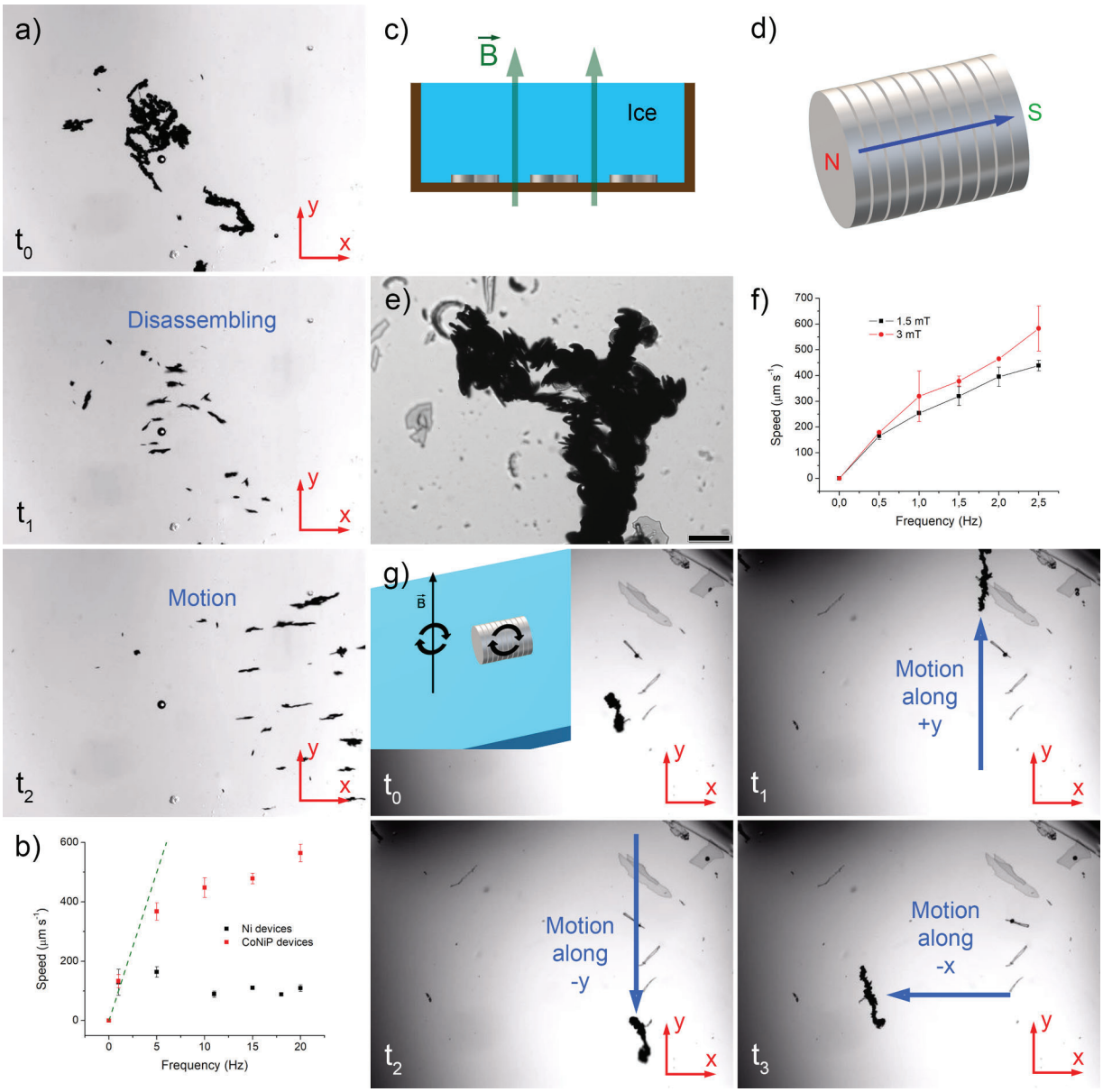

Fig. 5. Magnetic disassembling of aggregates of CoNiP devices (a); relationship between the linear speed of the aggregates and the frequency used for their actuation (b); approach employed to program the magnetization axis of the CoNiP devices (c); scheme (d) and experimental verification (e) of the behaviour of perpendicularly magnetized CoNiP samples; speed of an aggregate of perpendicularly magnetized CoNiP samples (f); controlled actuation of an aggregate of perpendicularly magnetized CoNiP samples (g).

device and keep the swimmer synchronized with the applied field. Apparently, an analogous effect takes place for the devices described in the present work. By increasing the external field, and therefore the torque applied, it is possible to avoid step-out at low frequencies.

When the devices were actuated at high frequencies according to an out of plane rotation, another interesting effect was observed. Due to the high speed of rotation, the bigger clusters dissembled in shorter chains. This phenomenon could be exploited to reduce the dimension of the aggregates and therefore limit the differential motion of the swarm. In Fig. 5a and Supporting Video 4 it is possible to observe this effect in the case of CoNiP devices actuated through a 15 mT field rotating clockwise around the y axis at a frequency of 20 Hz.

3.7. Magnetic programming of the CoNiP devices

Thanks to their good remanence, the CoNiP devices can be permanently magnetized along any arbitrary axis. Moreover, their coercivity is high enough to avoid demagnetization under the relatively mild magnetic fields employed for their actuation (max 15 mT). As a consequence, the magnetic behavior of the micromotors can be programmed. The main difficulty that must be overcome in order to do this is connected with the easy axis of the devices. If immersed in a magnetic field without being fixed in a specific orientation, the cylinders always orient along their easy axis, making impossible the imposition of an arbitrary magnetization. The present work utilizes ice to overcome this challenge (Fig. 5c). The devices, under the influence of gravity, lay flat on the bottom of the arena used for their actuation. If the arena is filled with water, the latter can be frozen, blocking the devices in a fixed position. In this way, it is possible to use a magnet positioned at an arbitrary angle with respect to the devices, to impart them a well-directed magnetization vector.

This was done for a swarm of CoNiP devices, which were magnetized along the out of plane direction (parallel to their symmetry axis, as visible in Figure S10), and a peculiar outcome was observed after the ice melting step. All the devices aggregated, forming a single block. This block did not present the typical morphology of aggregates resulting from in plane magnetized devices, where the single devices were in contact in correspondence of their external edges. Magnetized CoNiP devices formed stacks with the devices prevalently touching on their flat faces (Fig. 5d). The resulting aggregate was relatively compact and hard to break with an external force (Fig. 5e).

This compact structure can be actuated applying rotating fields in a way similar to the aggregates previously discussed. Fig. 5g and Supporting Video 5 show the outcome of a typical actuation test carried out on an aggregate of magnetically programmed CoNiP devices. Initially, at t_1, the rotation of the external magnetic field was set anticlockwise around the x axis. As a consequence, the aggregate tumbled along the y direction. Then, at t_2, the field was set to rotate clockwise around the x axis and the aggregate inverted its motion and moved opposite to the y direction. Finally, at t_3, the field was set to rotate clockwise around the y axis and the aggregate started moving opposite to the x direction. The speed of the device as a function of the rotation frequency of the external field is described by Fig. 5f.

3.8. PPy coated microdevices for drug delivery

In order to provide an applicative perspective to the swarms of disk-shaped devices described in the present work, they were functionalized with polypyrrole in order to carry out drug delivery tasks. The materials constituting the devices, Ni and CoNiP, are not biocompatible, but the experimentation carried out simply aims at demonstrating that the disk-shaped micromotors here described can be successfully functionalized with a functional polymer, loaded with a model molecule and used for controlled release of the molecule itself.

Polypyrrole was applied by immersing the devices into a bath containing pyrrole and ammonium persulfate. The latter acts as an oxidant and starts the polymerization of pyrrole according to the following reaction:

$$C_4H_4NH + (NH_4)_2S_2O_8 \rightarrow [C_4H_2NH]_n + H_2SO_4 + (NH_4)_2SO_4$$

Fig. 6a and 6b shows the morphology of the obtained PPy layer observed at the SEM. The device appears uniformly covered by PPy, whose thickness was estimated to be around 1 μm. The layer presents some inhomogeneities and the thickness is not perfectly constant all over the surface. Some cracks are visible where it is higher. Fig. 6c shows the element distribution of the sample visible in Fig. 6a, demonstrating the presence of PPy on the surface of the device.

The result of the drug release test carried out is reported in Fig. 6d. The swarm of devices successfully stored and then released RhB over a time span of 2 h. Such release can be modelled using a simple first order kinetic model, represented by Eq. (8).

$$\frac{dC}{dt} = -kC \tag{8}$$

C is the concentration of RhB in the environment, while k is the kinetic constant for the release process. By integrating Eqs. (8) and (9) can be obtained.

$$\frac{C_t}{C_\infty} = 1 - e^{-kt} \tag{9}$$

C_t is the concentration at time t, while C_∞ is the terminal concentration at the end of the release process (for $t \rightarrow \infty$).

Eq. (9) was used to fit the data reported in Fig. 6d. In this way, the terminal concentration C_∞ was estimated at 32.59 μg l^{-1} and the release constant k was estimated at 0.032 s^{-1}. However, the R-square for the fitting was 0.944, suggesting a limited quality of the fitting. By carefully considering the fitting obtained (Figure S11), it can be seen that the main liming factor for its quality is the value at time 0, since the concentration of RhB at time 0 is expected to be 0. It is therefore possible that the release observed during the test was characterized by some degree of burst release [57,58]. Under this phenomenon, the devices instantaneously release a small percentage of the molecule they contain. To take into account this effect, Eq. (9) was corrected by adding C_b, the concentration instantaneously reached at the beginning of the release test (Eq. (10)).

$$C_t = C_b + C_\infty\left(1 - e^{-kt}\right) \tag{10}$$

In this way, the R-square for the fitting improved to 0.979. The burst release concentration C_b resulted equal to 3.44 μg l^{-1}, the terminal concentration C_∞ was estimated at 32.59 μg l^{-1} and the release constant k was estimated at 0.021 s^{-1}.

4. Conclusions

Disk-shaped micromotors were successfully manufactured employing a novel combination of inkjet assisted lithography and electroforming. This hybrid technique enables the production of large amounts of devices with a controllable diameter and thickness. The magnetic properties of the ferromagnetic micromotors can be tuned by carefully selecting the electroformed material. As an example of soft magnetic material, Ni was used, while CoNiP was used as a representative example of semi-hard magnetic material. Following their production, the ferromagnetic devices were actuated in large swarms containing many of them. It was shown that soft magnetic devices self-assemble into linear aggregates, which can be manipulated employing rotating magnetic fields. The length of the aggregates followed a dispersed distribution and demonstrated faster speed for longer chains. While this can enable more versatile control strategies enabling multiple speeds under the same applied magnetic fields, some applications might require uniform control of the collection of aggregates. For such cases, hard-magnetic devices can be utilized, since high-frequency rotations of the

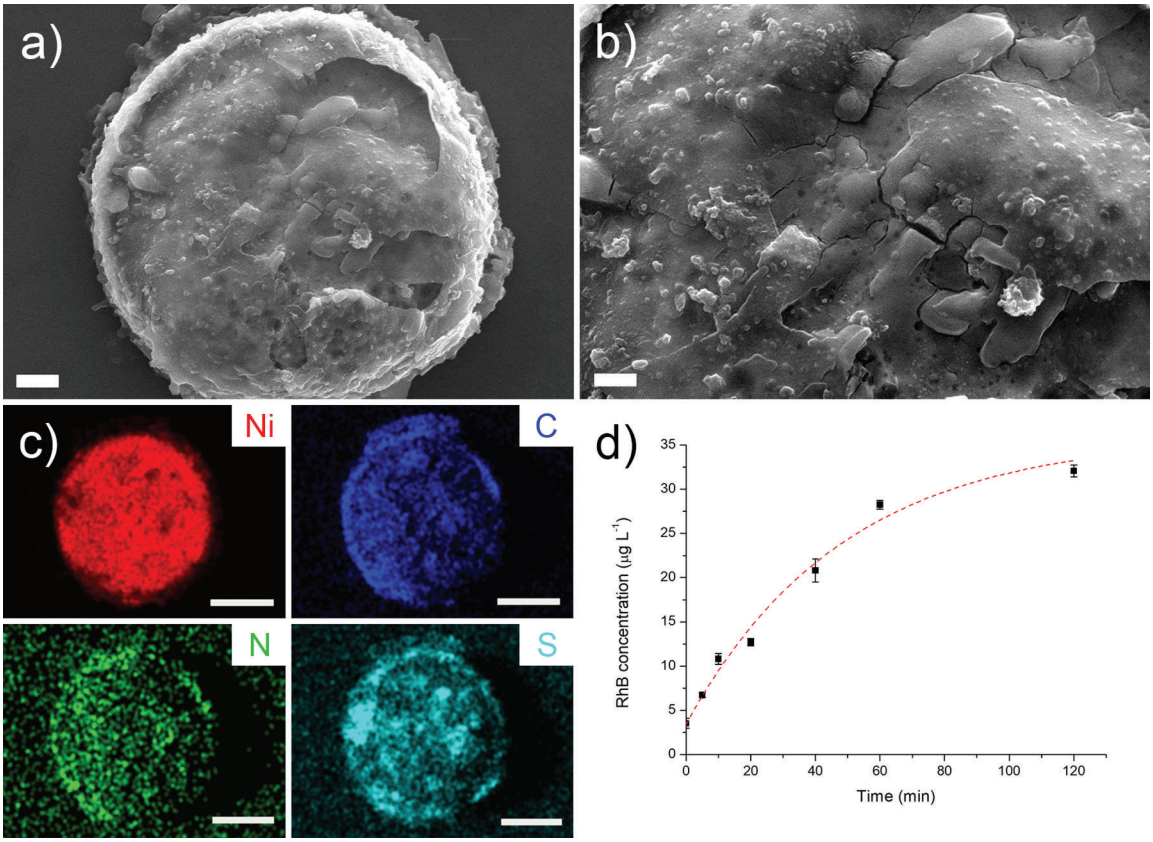

Fig. 6. SEM characterization of a PPy coated Ni device (a, scale bar = 4 μm; b, scale bar = 2 μm)); elemental mapping for Ni, N, C and S of a PPy coated device (c, scale bar = 20 μm); RhB release test performed on a swarm of PP coated Ni devices (d).

magnetic fields can allow for partial disassembly. Indeed, the differential motion of the swarm can be mitigated, in the case of semi-hard magnetic devices like the CoNiP made ones, using high rotation frequencies for the magnetic field. Under these conditions, a partial disassembling of the aggregates take place, which narrows the size distribution of the aggregates and consequently their speed distribution. On the other hand, differential motion can be totally eliminated by programming the magnetization axis of the CoNiP devices. Indeed, when they are magnetized along their hard magnetic axis, they self-assemble into a compact mass of devices, which can be actuated as a single block. The devices constituting the block maintain their swarm-like properties (like a high specific area, useful for drug delivery), but they move as a single entity. In addition, if the coercivity of the material is properly tuned, the aggregate can be disassembled by applying a strong magnetic field. The results obtained demonstrate the potentialities of the IAL/electroforming technique for the production of disk-shaped micromotors and their theoretical capabilities as smart drug carriers able to efficiently transport and release chemical species.

CRediT authorship contribution statement

Roberto Bernasconi: Writing – review & editing, Writing – original draft, Visualization, Methodology, Investigation, Formal analysis, Conceptualization. **Anna Nova:** Writing – original draft, Validation, Methodology, Investigation, Formal analysis. **Buse Aktas:** Writing – review & editing, Visualization, Validation, Data curation. **Salvador Pané:** Writing – review & editing, Validation, Supervision, Software, Resources, Project administration. **Luca Magagnin:** Supervision, Software, Resources, Project administration.

Declaration of competing interest

The authors declare that they have no known competing financial interests or personal relationships that could have appeared to influence the work reported in this paper.

Data availability

Data will be made available on request.

Supplementary materials

Supplementary material associated with this article can be found, in the online version, at doi:10.1016/j.apmt.2024.102365.

References

[1] M. Sitti, Miniature soft robots - road to the clinic, Nat. Rev. Mater. 3 (2018) 74–75, https://doi.org/10.1038/s41578-018-0001-3.
[2] F. Soto, E. Karshalev, F. Zhang, B. Esteban Fernandez de Avila, A. Nourhani, J. Wang, Smart Materials for Microrobots, Chem. Rev. (2021).
[3] M. Sitti, Voyage of the microrobots, Nature 458 (2009) 1121–1122.
[4] B.J. Nelson, I.K. Kaliakatsos, J.J. Abbott, Microrobots for Minimally Invasive Medicine, Annu. Rev. Biomed. Eng. 12 (2010) 55–85, https://doi.org/10.1146/annurev-bioeng-010510-103409.
[5] D. Jang, J. Jeong, H. Song, S.K. Chung, Targeted drug delivery technology using untethered microrobots: a review, J. Micromech. Microeng. 29 (2019) 53002.
[6] M.P. Kummer, J.J. Abbott, B.E. Kratochvil, R. Borer, A. Sengul, B.J. Nelson, Octomag: an electromagnetic system for 5-DOF wireless micromanipulation, IEEE Trans. Robot. 26 (2010) 1006–1017, https://doi.org/10.1109/TRO.2010.2073030.
[7] F. Qiu, B.J. Nelson, Magnetic helical micro-and nanorobots: toward their biomedical applications, Engineering 1 (2015) 21–26.

[8] J. Park, C. Jin, S. Lee, J. Kim, H. Choi, Magnetically actuated degradable microrobots for actively controlled drug release and hyperthermia therapy, Adv. Healthc. Mater. 8 (2019) 1900213.

[9] K.M. Sivaraman, G. Chatzipirpiridis, B. Becsek, T. Lühmann, O. Ergeneman, B. J. Nelson, S. Pané, Functional polypyrrole coatings for wirelessly controlled magnetic microrobots, in: IEEE EMBS Spec. Top. Conf. Point-of-Care Healthc. Technol. Synerg. Towar. Better Glob. Heal. PHT 2013, 2013, pp. 22–25, https://doi.org/10.1109/PHT.2013.6461275.

[10] R. Bernasconi, N. Favara, N. Fouladvari, M. Invernizzi, M. Levi, S.P. Vidal, L. Magagnin, Nanostructured Polypyrrole layers implementation on magnetically navigable 3D printed microdevices for targeted gastrointestinal drug delivery, Multifunct. Mater (2020).

[11] L. Yang, L. Zhang, Motion control in magnetic microrobotics: from individual and multiple robots to swarms, Annu. Rev. Control. Robot. Auton. Syst. 4 (2021) 509–534.

[12] K. Yuan, M. Pacheco, B. Jurado-Sánchez, A. Escarpa, Design and control of the micromotor swarm toward smart applications, Adv. Intell. Syst. 3 (2021) 2100002.

[13] M. Fernández-Medina, M.A. Ramos-Docampo, O. Hovorka, V. Salgueiriño, B. Städler, Recent advances in nano-and micromotors, Adv. Funct. Mater. 30 (2020) 1908283.

[14] P.J. Vach, D. Walker, P. Fischer, P. Fratzl, D. Faivre, Pattern formation and collective effects in populations of magnetic microswimmers, J. Phys. D. Appl. Phys. 50 (2017) 11LT03.

[15] S. Fu, D. Fu, D. Xie, L. Liu, B. Chen, Y. Ye, D.A. Wilson, F. Peng, Light driven micromotor swarm for tumor photothermal therapy, Appl. Mater. Today. 26 (2022) 101348.

[16] V. de la Asunción-Nadal, D. Rojas, B. Jurado-Sánchez, A. Escarpa, Transition metal dichalcogenide micromotors with programmable photophoretic swarming motion, J. Mater. Chem. A. 11 (2023) 1239–1245.

[17] J. Zhang, A. Laskar, J. Song, O.E. Shklyaev, F. Mou, J. Guan, A.C. Balazs, A. Sen, Light-powered, fuel-free oscillation, migration, and reversible manipulation of multiple cargo types by micromotor swarms, ACS Nano 17 (2022) 251–262.

[18] Z. Li, S. Fu, H. Li, B. Chen, D. Xie, D. Fu, Y. Feng, C. Gao, S. Liu, D.A. Wilson, Light-driven micromotor swarm induced in-situ polymerization and synergistic photothermal therapy, Chem. Eng. J. 468 (2023) 143393.

[19] B. Wu, D. Rivas, S. Das, Upstream mobility and swarming of light activated micromotors, Mater. Adv. (2023).

[20] Z. Liang, H. Joh, B. Lian, D.E. Fan, Light-stimulated micromotor swarms in an electric field with accurate spatial, temporal, and mode control, Sci. Adv. 9 (2023) eadi9932.

[21] X. Lu, Y. Wei, H. Ou, C. Zhao, L. Shi, W. Liu, Universal control for micromotor swarms with a hybrid sonoelectrode, Small 17 (2021) 2104516.

[22] X. Lu, H. Shen, Y. Wei, H. Ge, J. Wang, H. Peng, W. Liu, Ultrafast growth and locomotion of dandelion-like microswarms with tubular micromotors, Small 16 (2020) 2003678.

[23] T. Si, Z. Wu, W. He, Q. He, Self-propelled predator-prey of swarming Janus micromotors, Iscience 26 (2023).

[24] K. Villa, L. Krejčová, F. Novotný, Z. Heger, Z. Sofer, M. Pumera, Cooperative multifunctional self-propelled paramagnetic microrobots with chemical handles for cell manipulation and drug delivery, Adv. Funct. Mater. 28 (2018) 1804343.

[25] M. Sun, X. Fan, X. Meng, J. Song, W. Chen, L. Sun, H. Xie, Magnetic biohybrid micromotors with high maneuverability for efficient drug loading and targeted drug delivery, Nanoscale 11 (2019) 18382–18392.

[26] X. Dong, M. Sitti, Controlling two-dimensional collective formation and cooperative behavior of magnetic microrobot swarms, Int. J. Rob. Res. 39 (2020) 617–638, https://doi.org/10.1177/0278364920903107.

[27] C. Huang, T. Xu, X. Wu, Leader-follower formation control of magnetically actuated Millirobots for automatic navigation, IEEE/ASME Trans. Mechatronics. 29 (2024) 1272–1282, https://doi.org/10.1109/TMECH.2023.3300010.

[28] T. Xu, Z. Hao, C. Huang, J. Yu, L. Zhang, X. Wu, Multimodal locomotion control of needle-like microrobots assembled by ferromagnetic nanoparticles, IEEE/ASME Trans. Mechatronics. 27 (2022) 4327–4338, https://doi.org/10.1109/TMECH.2022.3155806.

[29] J. Yu, T. Xu, Z. Lu, C.I. Vong, L. Zhang, On-demand disassembly of paramagnetic nanoparticle chains for microrobotic cargo delivery, IEEE Trans. Robot. 33 (2017) 1213–1225.

[30] J. Yu, L. Yang, L. Zhang, Pattern generation and motion control of a vortex-like paramagnetic nanoparticle swarm, Int. J. Rob. Res. 37 (2018) 912–930.

[31] J. Yu, B. Wang, X. Du, Q. Wang, L. Zhang, Ultra-extensible ribbon-like magnetic microswarm, Nat. Commun. 9 (2018) 3260.

[32] C.E. Sing, L. Schmid, M.F. Schneider, T. Franke, A. Alexander-Katz, Controlled surface-induced flows from the motion of self-assembled colloidal walkers, Proc. Natl. Acad. Sci. 107 (2010) 535–540.

[33] H. Xie, M. Sun, X. Fan, Z. Lin, W. Chen, L. Wang, L. Dong, Q. He, Reconfigurable magnetic microrobot swarm: multimode transformation, locomotion, and manipulation, Sci. Robot. 4 (2019) 1–15, https://doi.org/10.1126/scirobotics.aav8006.

[34] T. Xu, C. Huang, Z. Lai, X. Wu, Independent Control Strategy of Multiple Magnetic Flexible Millirobots for Position Control and Path Following, IEEE Trans. Robot. 38 (2022) 2875–2887, https://doi.org/10.1109/TRO.2022.3157147.

[35] R. Bernasconi, G. Prioglio, M.C. Angeli, C.C.J. Alcantara, S. Sevim, S. Pané, P. Vena, L. Magagnin, Wet metallization of 3D printed microarchitectures: application to the manufacturing of bioinspired microswimmers, J. Manuf. Process. 78 (2022) 11–21, https://doi.org/10.1016/j.jmapro.2022.03.057.

[36] H. Li, Microfabrication techniques for producing freestanding multi-dimensional microstructures, Microsyst. Technol. 22 (2016) 223–237.

[37] E. Tekin, P.J. Smith, U.S. Schubert, Inkjet printing as a deposition and patterning tool for polymers and inorganic particles, Soft Matter 4 (2008) 703–713.

[38] B. Bao, J. Jiang, F. Li, P. Zhang, S. Chen, Q. Yang, S. Wang, B. Su, L. Jiang, Y. Song, Fabrication of patterned concave microstructures by inkjet imprinting, Adv. Funct. Mater. 25 (2015) 3286–3294.

[39] C.W. Sele, T. Von Werne, R.H. Friend, H. Sirringhaus, Lithography-free, self-aligned inkjet printing with sub-hundred-nanometer resolution, Adv. Mater. 17 (2005) 997–1001.

[40] K.V. Nemani, K.L. Moodie, J.B. Brennick, A. Su, B. Gimi, In vitro and in vivo evaluation of SU-8 biocompatibility, Mater. Sci. Eng. C. 33 (2013) 4453–4459.

[41] V. Fakhfouri, N. Cantale, G. Mermoud, J.Y. Kim, D. Boiko, E. Charbon, A. Martinoli, J. Brugger, Inkjet printing of SU-8 for polymer-based MEMS a case study for microlenses, in: Proc. 21st IEEE Int. Conf. Micro Electro Mech. Syst. 2008, IEEE, 2008, pp. 407–410.

[42] J. Greener, W. Li, J. Ren, D. Voicu, V. Pakharenko, T. Tang, E. Kumacheva, Rapid, cost-efficient fabrication of microfluidic reactors in thermoplastic polymers by combining photolithography and hot embossing, Lab Chip 10 (2010) 522–524.

[43] R. Bernasconi, M.C. Angeli, F. Mantica, D. Carniani, L. Magagnin, SU-8 inkjet patterning for microfabrication, Polymer (Guildf) 185 (2019) 121933, https://doi.org/10.1016/j.polymer.2019.121933.

[44] R. Bernasconi, A. Nova, S. Pané, L. Magagnin, Electrodeposition of Equiatomic FePt permanent magnets from non-aqueous electrolytes based on ethylene glycol, J. Electrochem. Soc. 169 (2022) 72506.

[45] M. Goiriena-Goikoetxea, D. Muñoz, I. Orue, M.L. Fernández-Gubieda, J. Bokor, A. Muela, A. García-Arribas, Disk-shaped magnetic particles for cancer therapy, Appl. Phys. Rev. 7 (2020), https://doi.org/10.1063/1.5123716.

[46] R. Mansell, T. Vemulkar, D.C.M.C. Petit, Y. Cheng, J. Murphy, M.S. Lesniak, R. P. Cowburn, Magnetic particles with perpendicular anisotropy for mechanical cancer cell destruction, Sci. Rep. 7 (2017) 1–7, https://doi.org/10.1038/s41598-017-04154-1.

[47] G. Gardi, S. Ceron, W. Wang, K. Petersen, M. Sitti, Microrobot collectives with reconfigurable morphologies, behaviors, and functions, Nat. Commun. 13 (2022) 1–14, https://doi.org/10.1038/s41467-022-29882-5.

[48] S. Pané, E. Pellicer, K.M. Sivaraman, S. Suriñach, M.D. Baró, B.J. Nelson, J. Sort, High-performance electrodeposited Co-rich CoNiReP permanent magnets, Electrochim. Acta. 56 (2011) 8979–8988, https://doi.org/10.1016/j.electacta.2011.07.138.

[49] E. Effati, B. Pourabbas, M.S. Zakerhamidi, Continuous microfluidic fabrication of polypyrrole nanoparticles, RSC Adv 9 (2019) 16977–16988.

[50] P. Xu, X. Han, C. Wang, D. Zhou, Z. Lv, A. Wen, X. Wang, B. Zhang, Synthesis of electromagnetic functionalized nickel/polypyrrole core/shell composites, J. Phys. Chem. B. 112 (2008) 10443–10448.

[51] H.Y. Gan, X. Shan, T. Eriksson, B.K. Lok, Y.C. Lam, Reduction of droplet volume by controlling actuating waveforms in inkjet printing for micro-pattern formation, J. Micromech. Microeng. 19 (2009), https://doi.org/10.1088/0960-1317/19/5/055010.

[52] D.Y. Park, N.V. Myung, M. Schwartz, K. Nobe, Nanostructured magnetic CoNiP electrodeposits: structure-property relationships, Electrochim. Acta. 47 (2002) 2893–2900, https://doi.org/10.1016/S0013-4686(02)00160-3.

[53] C. Bi, M. Guix, B.V. Johnson, W. Jing, D.J. Cappelleri, Design of microscale magnetic tumbling robots for locomotion in multiple environments and complex terrains, Micromachines (Basel) 9 (2018) 68–85.

[54] B. Yigit, Y. Alapan, M. Sitti, Programmable collective behavior in dynamically self-assembled mobile microrobotic swarms, Adv. Sci. 6 (2019) 1801837.

[55] L. Zhang, J.J. Abbott, L. Dong, K.E. Peyer, B.E. Kratochvil, H. Zhang, C. Bergeles, B. J. Nelson, Characterizing the swimming properties of artificial bacterial flagella, Nano Lett 9 (2009) 3663–3667, https://doi.org/10.1021/nl901869j.

[56] M.A. Zeeshan, R. Grisch, E. Pellicer, K.M. Sivaraman, K.E. Peyer, J. Sort, B. Özkale, M.S. Sakar, B.J. Nelson, S. Pané, Hybrid helical magnetic microrobots obtained by 3D template-assisted electrodeposition, Small 10 (2014) 1284–1288, https://doi.org/10.1002/smll.201302856.

[57] S. Bhattacharjee, Understanding the burst release phenomenon: toward designing effective nanoparticulate drug-delivery systems, Ther. Deliv. 12 (2021) 21–36.

[58] N. Abbasnezhad, M. Kebdani, M. Shirinbayan, S. Champmartin, A. Tcharkhtchi, S. Kouidri, F. Bakir, Development of a model based on physical mechanisms for the explanation of drug release: application to diclofenac release from polyurethane films, Polymers (Basel) 13 (2021), https://doi.org/10.3390/polym13081230.